LAWRENCE
LIVERMORE
NATIONAL
LABORATORY

LLNL-JRNL-647302

The Role of Electronic Defects and Brittle Microstructure in Laser-Driven Material Failure

R. N. Raman, S. Elhadj, T. A. Laurence, M. J. Matthews

December 6, 2013

JOURNAL OF PHYSICS D-APPLIED PHYSICS

Disclaimer

The role of electronic defects and brittle microstructure in laser-driven material failure

R N Raman*, S Elhadj, T A Laurence and M J Matthews

Lawrence Livermore National Laboratory, 7000 East Ave., Livermore, California 94551

**raman4@llnl.gov*

The microstructural thermal response of fused silica subjected to laser-induced breakdown was investigated. Rapid thermal annealing of laser modified material at the surface was achieved using a CO_2 laser, and the relaxation response of photoluminescence, infrared (IR) reflectance, electron, and white light microscope images were recorded. Subsequent nanosecond pulsed laser damage threshold measurements revealed thermally-driven kinetics which were dominated by absorbing defect annealing at heat treatment temperatures (T_{HT}) below ~1200 K and material toughening at higher T_{HT}. A decrease in the peak photoluminescence lifetime with T_{HT} revealed two types of defects which were correlated with non-bridging IR vibrational modes. Near the glass transition temperature, a weakening of the laser modified material was observed and explained in terms of a residual compressive stress relaxation. A nonlinear absorption model was used to predict optical breakdown threshold and compared with critical fracture predictions based on crack tip annealing. Combined with a qualitative stress relaxation analysis, our model agrees well with the experimental data and yields insight to the rate-limiting contributions driving the onset of laser-induced breakdown in defective silica.

Subject Classification Numbers: 42.70.Ce, 78.55.Qr, 78.30.-j, 81.40.Ef, 81.40.Tv, 65.60.+a, 81.40.Np

1. Introduction

Demand for increased output from high-power laser systems is driven by a number of technologies including ultraviolet (UV) lithography, micromachining, and laser-driven inertial confinement fusion (e.g., Laser MegaJoule and National Ignition Facility). The corresponding energy densities are ultimately limited by the susceptibility of the internal optical components to laser-induced breakdown. In particular, localized breakdown at the surface of fused silica under nanosecond-pulsed laser conditions can lead to the formation of a crater and associated subsurface cracks (collectively referred to as a *damage site*) [1]. Though such a site is typically only a few to few tens of microns in diameter when created [2], if left without intervention it can grow large enough to render even a large (1000 cm^2) optic unusable [3]. In the case of high quality, occlusion-free large aperture optics, replacement can be costly.

Recent improvements in post-processing technology have resulted in fused silica optics which exhibit an order of magnitude fewer damage sites [4]. Because of this reduced number of sites per optic, the ability to repair individual sites has the potential to extend the useful lifetime of large aperture optics by more than a factor of ten. For example, it has been known for some time that surface heating using a continuous wave (cw) CO_2 laser increases resistance to damage initiation by nanosecond pulsed laser exposure compared to that of conventional mechanically polished optics [5]. Despite this early discovery, the mechanisms involved in damage threshold increase from such laser 'fire polishing' have never been established, nor has there been a systematic study linking changes in material properties to direct thermal characterization. It was later demonstrated that CO_2 laser polishing of an already existing SiO_2 surface damage site can increase its resistance to damage by UV laser pulses and therefore arrest growth [6]. CO_2 laser exposure in this sub-ablation threshold regime was later identified with local flow and redistribution of the material in the damaged volume [7-9]. However, it is not known how these modifications in the microstructure directly relate to the observed increase in damage threshold fluence (φ_{th}).

Several mechanisms that may be responsible for the re-initiation of damage of optical materials subject to high average power nanosecond laser exposure have been suggested. In particular, 1) local

intensification of the incident light field due to irregular optical surface morphology [10, 11], 2) absorption of incident laser pulse energy via the presence of electronic defects[12], followed by local heating [13], expansion, and magnification of the stress intensity factor, and 3) decrease in the fracture toughness due to the higher density of micro-cracks in the damaged material [14] all may lead to damage re-initiation. Although each of these can interact with the others in a complex manner, we hypothesize that they manifest with distinct structural relaxation behaviors as a function of heat treatment temperature (T_{HT}) and time (t_{HT}).

For example, in a previous study we found an inverse correlation between the peak T_{HT} of a CO_2 laser-irradiated damage site and photoluminescence intensity for a constant t_{HT}, revealing distinct relaxation behaviors of electronic defects being probed under different UV excitation wavelengths [15]. Damage that disrupts bonds and modifies the local electronic structure of pristine silica (intrinsic band gap ~9 eV) can generate such optical absorption states at energies of just a few eV. These sub-band gap states were originally detected in the silica bulk [8], but similar states have also been found at the surface and are treatable by local CO_2 laser heating [16, 17].

A number of studies have focused on generating the theoretical framework for CO_2-laser based mitigation of laser-induced damage in fused silica [18-20]. None, however, have included all of the previously proposed phenomena presently known to occur in the glass substrate during damage, namely influence of cracks, local stress, absorber concentration and distribution, and local light intensification.

In this work, we critically assess the onset of nanosecond pulsed laser damage and identify three distinct annealing regimes of defective fused silica as expressed in the complex φ_{th} dependence on T_{HT} and t_{HT}. This complex dependence arises from the co-occurrence of morphological, mechanical, and electronic structure relaxation that can be antagonistic. We probe the thermal kinetics of these microstructural modifications under rapid (relative to conventional oven-based) thermal anneal using temporally and spectrally-resolved optical spectroscopy and relate the results to measured UV laser-induced breakdown threshold. Photoluminescence (PL) and μm-scale spatial resolution Fourier transform infrared (FTIR) spectroscopy reveal two distinct defect populations which anneal with different kinetics.

At low annealing temperature and short heating time, the laser-induced breakdown threshold of damaged silica depends mainly on the annealing of photo-active defects. Under more aggressive annealing conditions, the damage threshold is determined by crack tip blunting and the resulting material strength increase. At intermediate annealing conditions a decrease in breakdown threshold is observed and explained in terms of stress relaxation. A theoretical model is developed and used to rationalize the experimental results and gives insight to the rate-limiting contributions to breakdown fluence as a function of thermal annealing conditions.

2. Experimental procedure

A regular array of localized laser-induced damage sites was created on the rear surface of a type III (Corning 7980, 800-1000 [OH] ppm by wt.) fused silica window by a focused 355 nm 7-nanosecond, 50 J/cm^2 pulse as described previously [21]. Initiated sites were then exposed to additional (3-4) pulses at ~10 J/cm^2 until grown to d_0 ~150 μm in diameter. An SEM micrograph of a typical grown damage site is displayed in Fig. 1(a). Each site was then exposed under ambient conditions to a rapid thermal anneal using a 10.6 μm continuous-wave (cw) CO_2 laser (Synrad Firestar V20, 1/e^2 beam diameter of 0.77 mm) as described in Section 2.1. Section 2.2 describes the photoluminescence measurements to characterize electronic defect density. Section 2.3 details microstructural characterization using synchrotron-based FTIR. Finally, Section 2.4 describes the pulsed laser damage testing and damage threshold determination methods.

2.1 Sample preparation

In situ thermal emission measurements based on a calibrated mercury cadmium telluride (MCT) camera were used to measure local CO_2 laser heat treatment temperature (T_{HT}) as described previously [22, 23]. Each site received a single exposure of $1100<T_{HT}<2250$ (±50) K and heat-treatment exposure time t_{HT} of 3 – 300 seconds, with n=8 sites per (T_{HT}, t_{HT}) group. These laser annealing conditions represent near steady-state heating in the treated area of our fused silica samples[22]. Each group was chosen so as

to span relevant critical surface temperatures (from below the glass transition temperature T_g ~1315 K for Type III silica to 2500 K, just below the onset of evaporation ~2800 K) and expected bulk relaxation kinetics of SiO_2 [24]. This range of treatment parameters reflects the large span (~10^{12} s) of shear relaxation times $\tau_R=\eta(T_{HT}/G)$ where η is viscosity and G=31 GPa is the shear modulus) under which damage annealing evolves. Owing to the relatively rapid annealing conditions (t_{HT} ~10's of s compared to several hours for an oven anneal), no devitrification was observed as a result of any of the thermal treatments. Additionally, 8 sites received no CO_2 laser heat-treatment and served as control. An SEM micrograph of a damage site distinct from that shown in Fig. 1(a) and treated at 2250 K for 30 s is shown in Fig. 1(b). Smoothing of crater features was observed in SEM images only for treatments ≥ ~1650 K.

2.2 Time-resolved photoluminescence spectroscopy

In order to estimate the residual concentration of electronic defects following annealing, a pulsed, focused laser beam (405 nm, 150 ps full width at half maximum, 20 MHz repetition rate) was used as a PL excitation source. A time-resolved histogram of the emission filtered above 450 nm was detected by a time-correlated single photon counting system described in detail elsewhere [25]. This choice of excitation-emission wavelength corresponds to absorption-emission of defects previously associated with UV laser-induced damage silica [16, 25]. While CO_2 laser exposure can theoretically drive off hydrogen from OH groups and generate dangling oxygen bonds on the undamaged surface, no additional PL due to CO_2 laser heating was observed. Time-resolved PL emission of silica flaws has been interpreted as being derived from a distribution of lifetimes [26]. Following this approach, the data were fit to the function obtained by convolving the instrument response function (IRF) with the following stretched exponential model

$$y = A\exp(-(t/\tau)^{\beta}) \tag{1}$$

using maximum likelihood estimator fitting in order to determine the relationship between treatment conditions and the nature of the lifetime decay. As β decreases from 1, the simple exponential becomes increasingly stretched.

In a separate measurement, the same excitation source was used to collect an emission spectrum from each site. The emission was delivered to a spectrometer (Acton 300i) and detected by an avalanche photodiode capable of single photon counting. This arrangement yielded a spectral range of 360 – 800 nm with resolution of 1 nm.

2.3 Synchrotron-based Fourier transform infrared spectroscopy

To determine microstructural features related to the molecular bond network of treated sites, μm-scale spatial resolution IR reflectivity measurements were performed at beam line 1.4.3 of the Advanced Light Source (ALS) at Lawrence Berkeley National Laboratory under ambient conditions. Coherent IR light from the synchrotron was directed through a Nicolet Magna 760 Fourier transform infrared (FTIR) interferometer bench with a KBr beam splitter and a Spectra Tech Nic-Plan IR microscope (32× objective, NA = 0.65, diffraction-limited spot size of ~10 μm). An MCT detector collected the reflected light over a frequency range of 650–4000 cm^{-1} with a spectral resolution of ~4 cm^{-1}. Sample images were acquired with an automated microscope stage (Prior ProScan II) with step size of 10 μm.

2.4 Damage testing with diagnostic imaging

Following PL and FTIR characterization, the local UV laser damage fluence threshold (φ_{th}) at each site was measured. Sites were exposed in vacuum (10^{-6} Torr) to a series of temporally flat 5-ns laser pulses of increasing fluence between 2.5-13.0 J/cm^2, in ~1J/cm^2 steps using a custom-built, large aperture (30 mm diameter) 351 nm laser system [27]. For sites that did not damage up to the 13 J/cm^2 system limit, the laser energy was focused down to a 17 mm diameter beam, allowing a local fluence of 14-30 J/cm^2. *Ex situ* high resolution microscopy (10×/0.28NA) was used to detect laser breakdown events on sites. The damage threshold φ_{th} was defined to be the mean laser fluence over a 500 μm × 500 μm square patch surrounding the damage site at which the site exhibited an increase in its initial diameter [28, 29]. Figure

1(c) shows an SEM micrograph of a damage site treated at 2200 K for 100 s. Inset is an optical micrograph of the site shown in c) prior to damage testing. Arrows are registered and correspond to the location where damage re-initiated.

3. Results

Section 3.1 presents the thermally-induced change in UV excited state population densities and lifetimes, identifying two distinct species contributing to optical emission. Section 3.2 associates these changes to the microstructure of silica, revealing two types of Si-O dangling bond defects. Section 3.3 presents UV laser damage threshold enhancement as a function of thermal anneal. Section 3.4 offers a thermo-mechanical model and analysis which combines optical defect absorption and crack tip blunting effects to predict optical damage threshold changes.

3.1 Evolution of excited state decay lifetimes

An example fit to the lifetime histogram of an untreated site, which does not obey a single lifetime-valued decay, is shown in Fig. 2(a). Rather, a distribution of lifetimes was expected based on the variety of defects found in laser-damaged silica [16, 25]. The background-subtracted PL intensity is shown in Fig. 2(b). Low treatment temperature (T_{HT}=1250 K) PL emission intensity was roughly half that of untreated sites. As T_{HT} approached the softening point (1860 K for Type III silica), total PL intensity began to substantially decrease to levels 2 orders of magnitude lower than that of the untreated sites. In addition, at a given T_{HT}, longer anneal exposure times reduced the PL emission intensity by ~2× for every 10× increase in t_{HT}. A more meaningful visualization of the effect of thermal treatment on PL lifetime is achieved by plotting the *distribution* of lifetimes derived from the fits. Assuming a Gaussian distribution of lifetimes, we see in Fig. 3(a) that for the case for t_{HT} = 30 s, the peak of the distribution tends to shift to shorter lifetimes with increasing T_{HT}, plotted explicitly in Fig, 3(b) (with the exception of the 100 s case and data at T_{HT} = 2250 K, the latter which exhibits significant noise). First, a negligible change in lifetime (300 K vs. 1250 K) is associated with a ~2× decrease in PL intensity, while a strong decrease in lifetime from ~2.1 to 0.7 ns (~0.7× decrease between 1250 K and 2250 K) is associated with a much larger

decrease in PL intensity (50×, Fig. 2(b)). This suggests that there may be multiple types of emitting defects within the UV laser damaged regions of fused silica.

To identify specific electronic defects, a PL spectrum from an untreated site is shown in Fig. 4. A broadband emission is observed under this excitation covering bands previously observed in spectra of laser-damaged silica: oxygen deficiency centers (ODC, centered at 2.7 eV), non-bridging oxygen hole centers (NBOHC, centered at 1.9 eV) [8, 16], and continuum-like sub-microsecond emission lifetime (broadband emission centered at 2.2 eV) [25], respectively.

Normalized FTIR microreflectance spectra of the core region of UV laser damage sites exposed to a range of T_{HT} for 30 s are shown in Fig. 5. The spectrum of untreated, as-received silica is shown, indicating three broad features in the frequency range 650 – 1400 cm^{-1}, corresponding to the Si-O-Si symmetric stretching vibration (ν_{SS} ~790 cm^{-1}), the transverse optic (TO) Si-O-Si asymmetric stretching vibration ($\nu_{AS\text{-}TO}$~1120 cm^{-1}) and the longitudinal optic (LO) Si-O-Si asymmetric stretching vibration ($\nu_{AS\text{-}LO}$ ~1250 cm^{-1}) [30]. We note that there was some degree of variation among damage sites, but that the additional features relative to the as-received case were generally consistent among them. As T_{HT} increases, a red shift and decrease of the $\nu_{AS\text{-}LO}$ mode intensity (relative to $\nu_{AS\text{-}TO}$ mode intensity) is observed. This $\nu_{AS\text{-}LO}$ mode intensity only starts to decrease significantly in the T_{HT} range where smoothing of the damage site became visible under SEM (~1650 K) and approaches that of as-received silica at 2250 K (Fig. 5). This observation is consistent with oblique angle scattering [30] from an irregular surface that is reduced as the morphology evolves toward planarity with decreasing viscosity. An unexpectedly large decrease in this mode occurs following the highest T_{HT}. This is perhaps due to the elimination of local roughness that is otherwise present at lower T_{HT} and which is also related to the dependence of what spatial frequencies can be smoothed at various T_{HT} and t_{HT} [9]. Thus, the $\nu_{AS\text{-}LO}$ mode serves as a sensitive probe of the morphology and microstructure which evolves with annealing.

Between 850 and 1050 cm^{-1}, additional structure was observed that was recently reported [31] which is not typical of as-received amorphous SiO_2. In particular, a weak shoulder is observed in the range

1000-1050 cm^{-1} that appears close to previously reported A_{2u} modes of UV laser shock-induced stishovite [32]. More distinctly, between 850 and 1000 cm^{-1} (shaded region of Fig. 5) a band is observable which has previously been attributed to non-bridging SiO vibration [31]. A low frequency (~875 cm^{-1}) and high frequency (~940 cm^{-1}) component of this band can be identified in the untreated spectrum. The low frequency component appears to quench under T_{HT}=1250 K thermal anneal while the high frequency component blue shifts and quenches for T_{HT}>1250 K annealing. Collectively, these bands decrease with both T_{HT} and t_{HT}.

3.2 Optical breakdown threshold enhancement

Figure 6 shows the damage threshold φ_{th} dependence on T_{HT} and t_{HT}. Sites which received no treatment (control) exhibited a mean φ_{th} of 4.9 ± 0.9 J/cm^2. The same value for φ_{th} was obtained for the mildest treatment conditions (T_{HT}, t_{HT}) = (1150 K, 3 s) and is the value to which all of the data converged at low T_{HT}. For long t_{HT} (>100 s), φ_{th} increased monotonically from this value with T_{HT}. However, for shorter t_{HT}, φ_{th} un-expectedly decreased for a T_{HT} interval before increasing again at high T_{HT}; for example, for the series at 30 s, a slight decrease in φ_{th} was observed at T_{HT} =1350 K (just above the glass transition temperature T_g ~1315 K for Type III silica) [33]. For even shorter times, this decrease was more significant and occurred at higher values of T_{HT} (1600 K for the 10 s series). This decrease in φ_{th} suggests a T_{HT} interval (~1500-1850 K) for t_{HT} on the order of 10 s or less over which the sites actually damage at a *lower* fluence than those left untreated. Furthermore, the slope of the φ_{th} curves vs. T_{HT} was progressively steeper for T_{HT} > 1750 K treatments. The differences in behavior of each of the curves of Fig. 6 suggest that there could be competing time- and temperature-dependent kinetics involved in the thermally-driven modification of the breakdown threshold as discussed later.

3.3 Modeling of optical breakdown and material strength

In Section 3.4.1 we apply a transient thermo-mechanical model explicitly incorporating the change in UV absorber concentration, temperature-dependent physical properties, and absorption due to free carriers. Section 3.4.2 uses the Inglis equation to estimate material strength based on an evolving crack

tip geometry. The fluence, absorber concentrations, tensile stresses, and fracture strengths of damaged silica are estimated by comparing the φ_{th} data to this model.

3.3.1 Laser energy deposition and thermal strain

Recently, a model for laser absorption, which includes a temperature-induced band collapse and electronic contribution to the thermal conductivity, was proposed to explain pulse length-dependent changes in initiated damage site morphology [34]. An initially-heated region which triggers an 'absorption front' dependent on laser intensity I was used to simulate a high absorptivity precursor in an otherwise featureless silica-air interface. In our case, the PL emission data suggests the presence of more than one defect precursor which can anneal away with heat treatment, but are in contact with less defective, as-received silica. Thus we model two zones within a damage site: one in the 'core' region with a single fixed absorption coefficient, β_c (for simplicity) producing a heat source $Q_c = \beta_c I$ and one with a temperature-dependent absorption coefficient $\beta_b(T)$ of bulk silica producing a heat source $Q_b = \beta_b I$. A schematic of the geometry near an absorbing core region is shown in left side of Fig. 7. The laser-driven heat transport equation is given in terms of a total heat source $Q = Q_c + Q_b$ by

$$\rho C_p \frac{\partial T}{\partial t} + \rho C_p \boldsymbol{u} \cdot \boldsymbol{\nabla} T = \boldsymbol{\nabla} \cdot (k \boldsymbol{\nabla} T) + Q \tag{2}$$

where ρ, C_p and k are the temperature-dependent mass density, heat capacity and thermal conductivity respectively. The temperature, T, associated with the nanosecond laser heating process discussed here and in what follows is not be confused with the previously described annealing temperature, T_{HT}. In this model radiation transport is neglected as noted previously [34]. The second term on the left includes heat transport due to elastic body motion in terms of the velocity field $\boldsymbol{u}$. Light-matter coupling is described by a simplified photon transport expression (Beer-Lambert absorption),

$$\frac{dI}{dz} = -\beta_{c,b} I \tag{3}$$

with incident radiation taken to be in the z-direction in our simulations. In terms of core region size, we

chose a 100 nm radius hemisphere, consistent with observed defect region thicknesses of mechanically-indented features [35]. In fact, the size of the core region had little effect on the peak temperatures but moved the location of the absorption front edge accordingly. Similarly, planar absorbing regions were studied, and the effect on peak temperatures was small compared with overall changes in β_c and I_0. An example of the simulated temperature profile for β_c=1.5x10^3 cm^{-1} and I_0=20 J/cm^2 after 2.5 ns of laser irradiation is shown in the right side of Fig. 7.

At the high temperatures generated by laser absorption (T~10^4 K), the mechanical behavior of silica will include viscoplastic and ductile response. In addition, a shock wave can be launched after rapid heating and plasma generation which is not included in our model. However, because brittle failure criterion in the damaged area might be achieved at much lower temperatures (<3000 K), we include only (linear) thermoelasticity in our model for stress induced by laser heating and limit any quantitative discussion of stress calculated with the finite element model to these lower temperatures. At higher transient temperatures where thermal runaway occurs (T>3000 K), the estimates for stress should serve as a *lower bound* to those expected from shock waves [36] . Calculated stress fields can then be compared with failure criterion derived from linear elastic fracture mechanics. The equations of elasticity to be solved are then

$$\rho \frac{\partial^2 \boldsymbol{u}}{\partial t^2} - \boldsymbol{\nabla} \cdot \boldsymbol{\sigma} = 0,$$

$$\boldsymbol{\sigma} = \mathbf{C}\colon (\boldsymbol{\epsilon} - \boldsymbol{I}\epsilon_{th}),\ \epsilon_{th} = \alpha\left(T - T_{ref}\right) \tag{4}$$

$$\boldsymbol{\epsilon} = \frac{1}{2}(\nabla \boldsymbol{u} + \nabla \boldsymbol{u}^T)$$

where $\boldsymbol{\sigma}$ and $\boldsymbol{\epsilon}$ are the isotropic stress and strain tensors respectively, $\mathbf{C}$ is the elasticity tensor and α is the coefficient of (volume) thermal expansion. Equation (2) and (4) are thus coupled through $\boldsymbol{u}$. All material properties for fused silica were taken from Ref. [24]. Equations (2)-(4) were solved numerically in a 2D axisymmetric geometry using COMSOL Multiphysics finite element analysis software. The model

domain consisted of a 2×2 μm sample with variable meshing of ~10,000 elements. For the heat transport equation, insulating boundary conditions were used on the side and exit surfaces, while the input surface was held at T=293.15 K. The photon intensity equation was solved with fixed values for $I = I_0$, the initial intensity. We imposed a fixed constraint at the input surface and free surfaces on other boundaries in solving the elastic equations. Figure 8 shows the peak axial temperature generated by a 5 ns pulse as a function of (log) core absorption coefficient, β_c and incident laser fluence. A steep increase in temperature can be observed at about 500 cm^{-1} for high fluence (~20 J/cm^2) and at about $4x10^3$ cm^{-1} for fluence in the range 2~5 J/cm^2. At higher fluence and/or higher β_c, a plateau in T near 15,000 K can be seen due to large contributions of electronic transport to heat losses. We note however, that at these high temperatures other heat loss processes such as evaporation and radiation will contribute implying that our high T results are an over-estimate. Nonetheless, our results are in good agreement with T values previously calculated using a T=8,000 K initiating temperature seed [37].

The absorbed laser energy leads to heating, plasma formation, launch of a shock wave and eventually (>1 ns) the propagation of a pressure wave outward from an absorbing region [38, 39]. Besides local breakdown from the aforementioned rapid absorption mechanisms, damage may 'grow' when stress fields generated at arbitrary temperatures overlap spatially with material most prone to fail, i.e. material containing pre-existing cracks. Because the macroscopic behavior of the failure is that of brittle fracture, we calculate the maximum mode 1 tensile stress generated from pulsed laser heating. Figure 9 displays the simulated principal hoop stress profile following a 2 GW/cm^2, 5 ns (10 J/cm^2) laser pulse with β_c=10^3 cm^{-1} and α=1.65 ppm/K. At the end of the laser pulse, a peak compressive (negative) stress of ~60 MPa occurs on axis at the location of the absorber (as expected) below the surface along with peak tensile (positive) stress at the surface ~150 nm off-axis. The temporal evolution of the maximum tensile hoop stress and temperature are plotted in Figs. 9 (b-c), respectively. From this simulation we see that peak stresses approach ~10 MPa for laser intensity less than 3 GW/cm^2 (15 J/cm^2) with maximum temperatures reaching ~2900 K. In contrast, the 3 GW/cm^2 case leads to tensile stresses in excess of 500 MPa as well

as thermal runaway. However, the high density of pre-existing cracks will compromise the effective strength of the damage site. We now consider this point in more detail.

3.4.2 Material strength and crack healing

The Inglis equation [40] can be used to describe the critical stress (σ_c) condition for crack propagation and ultimately the failure criterion for brittle materials in terms of crack morphology and the theoretical strength σ_{th} of a material:

$$\sigma_c > \frac{\sigma_{th}}{2}\sqrt{\frac{R}{c}} \tag{5}$$

In Eq. 5 above, *c* is the length of an idealized notch within a continuous brittle material and *R* is the radius of curvature of the crack tip in the notch. Though the Griffith model [41] is perhaps a more widely used alternative for brittle failure criterion, the Inglis equation contains explicit information on crack tip morphology which has been argued crucial for a thermodynamically consistent model [42]. Furthermore, while a more complete description of crack tip stresses can be achieved using atomistic modeling [43], our goal is to capture the essential features of the crack morphology-stress relationship as it pertains to laser damage threshold. Specifically, Eq. 5 quantifies the stress concentration $\kappa = 2\sqrt{c/R}$, at the crack tip where the applied load is magnified, causing the material to fail far below its theoretical limit. For example, as a result of polishing-induced micro-fracture, the aforementioned tensile strength of an as-received silica slab is ~50 MPa, whereas the theoretical strength is σ_{th}~25 GPa implying κ~500. With a fracture toughness of 0.75 MPa√m for silica, this tensile strength implies a crack length of 145 μm. We have previously evaluated the critical stress criterion for laser-induced damage and found the crack length to be roughly equal to the average damage site diameter [24, 44]. Thus, we expect the yield point of the untreated damage site studied here to fall in the range 50~75 MPa. Referring to Fig. 9, we expect then that a critical stress is only achieved for absorptivity-fluence pairs which lead to thermal runaway. However, for annealed sites, the critical stress threshold can increase due to changes in crack morphology as discussed below.

For $T_{HT}>>T_g$ the viscosity of fused silica decreases to the point where capillary forces and surface diffusion will start to affect surface morphology [45]. Cracks will recede with blunting at the crack tip, and fuse together, until no cracks remain and the surface is smooth and devoid of cleaved-like features [46, 47]. In terms of fracture strength or brittle failure criteria, Eq. 5 implies that κ will decrease from a decrease in *c,* an increase in *R,* or both. We postulate that at the onset of annealing, crack tip blunting will first drive decreases in κ, owing to the short (~nm) length scales of the crack tip. A simple formalism for estimating morphological changes of a periodic structure due to annealing was proposed previously by Mullins, where capillarity, diffusion and evaporation-induced smoothing was cast in terms of spatial filtering in the frequency domain [9]. Despite the expectation that surface diffusion could be important in general, recent studies suggest that at submicron length scales, capillarity is the dominant surface smoothing mechanism for heated (~1700 K) silica surfaces [45, 48]. Under such conditions, the rate of change of the surface height *S* under annealing is expressed as

$$\frac{dS}{dt} = -\frac{\pi\gamma}{\eta}\nu S \tag{6}$$

where γ is the surface energy, η is the viscosity, and ν is the spatial frequency. Generally γ is a weak function of temperature in the temperature range studied here, so consider it a constant γ=0.3 N/m^2 [49]. Fused silica viscosity, however, varies as an Arrhenius with temperature as $\eta = \eta_0 \exp(E_a/RT)$ where we take η_0 =3x10^{-10} Pa·s and E_a=603 kJ/mole from recent measurements of laser induced surface smoothing [45]. An idealized 1D saw tooth surface with 44.5^o slopes was chosen to simulate a crack in evaluating Eq.(6) numerically [50]. The initial crack tip radius was 1.1 nm, as inferred by combining the Griffith and Inglis equations for brittle failure. Taken together, Eqs. (5) and (6) allow us to estimate the effect of crack tip healing on strength to assess its impact on the laser damage threshold.

4. Discussion

The SEM images of Fig. 1 suggest a distinct difference in the nature of the damage that occurs near the low T_{HT}, near-constant fluence regime vs. the high T_{HT} regime of the damage threshold curve (Fig.6). In Fig. 1(a) the large lateral crack seen in the upper left corner of the site represents a mechanically weak region and likely propagates at stresses achieved long before evaporative temperatures. In comparison, the re-initiated damage of Fig. 1(c) occurred at a fluence of 7 J/cm^2, above the 4.9 J/cm^2 baseline, and on a smoother, mechanically stronger surface devoid of fracture.

We discuss the laser-induced mechanical strengthening and defect healing portions of the model to determine their relative contributions to the enhancement in fluence threshold. From a material response standpoint, it is instructive to unify the temperature and time variables into a dimensionless material state variable $\delta \equiv t_{HT} G/\eta$. Figure 10 displays a comparison of the damage threshold behavior and predicted strength (c=100 μm) behavior as a function of δ. The log-log plots for φ_{th} and σ_f shown span a scale of 2 to 42 J/cm^2 and 20 to 420 MPa, respectively. Our model is represented by the solid line of the strength plot.

It is interesting to compare our results to those of Hirao and Tomozawa [14] who modeled the failure strength, σ_f, of abraded silicate samples as a function of annealing time, t and temperature T as

$$\sigma_f = \frac{\sigma_{th}}{2}\left(\frac{a}{2c}\right)^{1/2}\left(\frac{3}{2\pi a}\frac{\gamma}{\eta(T)}t + B\right)^{1/3} \quad (7)$$

where a is the crack radius (proportional but not equal to crack tip radius) and B is a constant on the order of unity determined by initial crack geometry. To compare with our crack tip blunting model in section 3.4.2, we consider a 100 μm crack length, B=1 and an initial strength of 41 MPa (a=2.3 nm). As shown, both our model and the Hirao model agree fairly well, with the latter increasing with δ more slowly due to the 1/3 power law dependence. For mild anneal conditions $\delta<10^3$, change in predicted crack morphology and hence damage site strength does not vary appreciably. This is to be compared with significant changes in φ_{th} for $10^{-5}<\delta<10^3$ where φ_{th} either decreases (t_{HT}=3, 10s) or increases (t_{HT}=30-300s). This observation leads us to the conclusion that crack tip blunting does not play a role in the damage threshold

improvement under these heat treatment conditions. Indeed, the lack of a unified dependence of φ_{th} on $\delta<10^3$ implies that simple capillarity is not the dominant physical phenomenon. However, the steep increase in φ_{th} for $\delta>10^3$ does, in fact, correlate well with the steep onset of capillary flow-induced strengthening. Furthermore, the similar dependence of φ_{th} vs. δ in this heat treatment regime also suggests that capillarity is a plausible mechanism for damage threshold increase at high (t_{HT}, T_{HT}). This predicted behavior in damage threshold can also be compared with direct strength measurements of ~100 μm indents on silicate glass surfaces subjected to thermal annealing [51] as shown by the symbols plotted in Fig. 10. Consistent with our model, strengthening due to crack tip blunting in those experiments did not occur for δ less than about 10^3~10^4.

Near δ~10^2, a dip occurs in the 3 and 10 s data which is not immediately addressed in any of our modeling so far. We rationalize this behavior as follows. Previously, a decrease in the laser damage threshold fluence of as-received silica was observed upon removal of a compressive stress load, suggesting that such an observed enhancement is stress-related [52]. Indeed, residual stresses have recently been observed in and around damage sites caused by successive UV laser damage events through birefringence measurements [53]. Therefore it is reasonable to assume that stress relaxation will influence damage threshold, depending on whether the stress field will stabilize or weaken regions of the damage site. Assuming Maxwellian viscoelastic behavior with simple rheological behavior [54], stress relaxation in silica glass will evolve as

$$\sigma_R(t,T) = \sigma_0 exp(-t/\tau_R) \tag{8}$$

where $\tau_R=\eta(T)/G$ is the shear stress relaxation time. For example, for a 100 s laser exposure that caused the glass temperature to rise to T~1315 K ($\eta=10^{13.6}$ Pa·s), the stress in the glass would relax to roughly 7.5% of its original value. Noting that δ is also equal to t_{HT}/τ_R, we plot σ_R/σ_0 in the graph of Fig. 10 associated with the right vertical scale, and compare it with the damage threshold behavior for δ~10^2. As shown, the decrease in damage threshold appears correlated with the calculated decrease in residual stress

that may be present in the damage site. Similar to the scaling argument given above for σ_f, the decrease in φ_{th} tends to scale with δ, supporting the idea that the effect is viscosity driven.

From Eq. 7 it can be shown that for high T_{HT} (T_{HT}>~1600 K), the term $3\gamma t/2\pi a\eta$ >> B and Hirao's crack tip blunting model predicts $\varphi_{th} \sim t_{HT}^{1/3}$. If we plot φ_{th} vs. t_{HT} on a log-log scale (Fig. 11), we see that around T_g, (specifically for the T_{HT} < 1580 K) there is no strong temporal dependence on φ_{th}. This could be expected since the proposed weakening of the material attributed to stress relaxation is countering the threshold enhancement due to electronic defect annihilation as discussed below. But at intermediate T_{HT} (1580-1680 K), a 1/3 power dependence does become apparent as expected by the Hirao model. At higher T_{HT} corresponding to the regime where crack tip blunting dominates damage sites strengthening, the t_{HT} dependence climbs beyond 1/3, agreeing (at least qualitatively) with our model.

Having related threshold to crack tip blunting under aggressive annealing conditions (large t_{HT}, T_{HT}) and stress relaxation at intermediary annealing conditions, we now consider the role of absorption in a system with no pre-existing cracks in order to model the 1) onset of a growth event and 2) threshold enhancement at treatment conditions well below those permitting capillary-driven crack tip blunting. Using our laser absorption-thermal model, we first note that the thermal runaway phenomenon is highly dependent on the value of the absorption coefficient in the core region, β_c. This establishes a natural threshold effect (φ_{th} vs. β_c) for a given laser intensity, as observed in Fig. 8 of section 3.4.1. That is, if β_c is too small, the precursor will heat, possibly inducing some densification but will not lead to explosive material vaporization and cracking. We intend to use this fact to explore how the annealing of optical defects should influence the damage threshold, assuming κ is constant. For φ_{th} = 4.9 J/cm^2, our thermal model (Fig. 8), would predict an absorbing core absorption coefficient of 2.1x10^3 cm^{-1}, assuming a temperature threshold equal to the boiling point of silica (~3000 K). We then assume that the measured PL intensities of Fig. 2 (I_{PL}) are linearly proportional to the concentration of defects and therefore scale with estimated absorption coefficient as $\beta_c = MI_{PL}$, where M = 0.24 cm^{-1} is the proportionality constant

determined from the intersection of the 3000 K isotherm with data from untreated sites (solid curve) and our laser absorption model Eq. 2.

Figure 12 plots φ_{th} as a function of β_c as derived from the total PL intensity measurements. For the T_{HT} range of 300-1250 K, the results from Figs. 2(b) and 6 show that the substantial decrease (~2×) in PL intensity (and therefore defect concentration n for a constant lifetime) was not accompanied by an expected decrease in φ_{th}: for $\log(\beta_c) > 5$, the thermal model (curves, Fig. 12) predicts a continued decrease in φ_{th} with increasing β_c in which the higher the density of absorbers generating heat, the lower the fluence necessary to heat SiO_2 above its boiling point. Instead, in this low T_{HT} limit, φ_{th} appears from experiment to clamp at ~4.9 J/cm^2 and suggests that other physical phenomena for absorption exist. It should be emphasized that the M-curves of Fig. 12 were derived solely from thermal runaway conditions, in which subsequent stresses cause failure, and do not depend on stresses from finite element modeling (which beyond thermal runaway are not well understood).

Due to the observed threshold phenomenon at higher absorber concentration, the treated sites do not lie along this same curve. Moreover, the data points in Fig. 12 corresponding to different time series do not overlap with each other when plotted against a generalized material parameter β_c, thus requiring modeling of additional kinetics regarding the defects or damage mechanism more generally to explain more completely. The 3000 K isotherm was then fitted to the various time series data (Fig. 12, dashed lines) and the best-fit value of M is indicated. Modifying M to 0.097 cm^{-1} shows good agreement with the low temperature φ_{th} observed in the 300 s series and its corresponding thermal runaway isotherm. In fact, good agreement continues through shorter t_{HT} series until the high T_{HT} case of the 10 s series and all data from the 3 s series. In these cases we note the onset of observed stress relaxation effects and poor agreement with failure by absorption alone. It is interesting to note that this deviation from 10 s data and model occurs after the shaded region corresponding to $\delta=10^3$, the normalized treatment time parameter value which marked the boundary between capillary-driven crack tip blunting and stress relaxation. This result further supports the dominance of each of these two phenomena in these respective regimes.

It is possible (and suggested by the observed PL spectra and stretched exponential lifetime distributions) that in fact multiple types of defects are present. This postulation is further supported by the two distinct temperature-dependent behaviors of the non-bridging oxygen modes observed in the FTIR spectra, namely the population that depletes with T_{HT} (mode at 875 cm^{-1}) and the population that blue shifts with T_{HT} (mode at 940 cm^{-1}). In an attempt to confirm the nature of these defects, we immersed unannealed laser damaged sites in 100% H_2 gas at room temperature and pressure to chemically probe the presence of NBO dangling bonds [55]. An 80% decrease in total PL was observed after ~30 minutes of soaking, consistent with hydrogen passivation of NBO defects typical at Si/SiO_2 interfaces of metal-oxide-semiconductors [56], followed by a slow (~18 hours) recovery to pre-soak PL levels. More interestingly UV damage tests, which were performed immediately after soak when PL was low, showed no significant increase in damage threshold expected from our model (Eq. 2). Hence we conclude that an NBO defect population around 875 cm^{-1} exists that is both PL active but un-related to laser induced breakdown. A more precise characterization of this defect population is ongoing and will be reported later. In contrast the modes around 975 cm^{-1} were previously observed in damage sites induced by nanosecond UV laser exposure of increasing pulse length [31]. It was proposed that the blue shift observed in that study may be due to the generation of a larger fraction of dangling bonds on the surface relative to bulk with increasing pulse length. Analogously, higher T_{HT} may be healing defects preferentially in the bulk compared to the exposed defects (fewer interactions) at the surface. Higher spatial resolution *in situ* spectroscopic measurements during laser annealing would permit a more detailed determination of relaxation mechanisms at the atomistic level.

In general, the existence of a φ_{th} limit at low T_{HT} suggests that the population being annealed does not contribute to damage and is dominated by *radiative* relaxation mechanisms. In this scenario, less of the absorbed UV pulse energy gets converted to catastrophic heat and a change in threshold fluence is not observed. Such an enhancement in PL efficiency has been detected in semiconductors despite relatively high (though inhomogeneous) defect density [57]. The shortening of the peak PL lifetime suggests that as the different defect types are healed with T_{HT}, they possibly become more interacting due to increased

mobility at higher T_{HT} despite healing and decreasing in absolute concentration.

5. Conclusions

Thermal annealing of laser modified SiO_2 was used to study microstructural defect evolution and relate the results to laser-induced breakdown threshold limits. Photoluminescence and infrared spectroscopy revealed two populations of defects which correlated with two annealing regimes of the laser modified material. Under slower annealing conditions (T_{HT}~1250 K, t_{HT}~300 s), the annihilation of absorbing defects was the dominant threshold enhancement contributor while at high T_{HT} material toughening caused by crack tip blunting is argued to play a more important role. Near the glass transition temperature, a weakening of the laser modified material was observed and explained in terms of a residual compressive stress relaxation. A nonlinear thermo-mechanical model was extended to include non-uniform absorber concentrations and used to predict optical breakdown threshold and generated stress fields. By estimating defect concentrations using measured PL, a reasonable agreement between model predictions and experiment was achieved.

Acknowledgments

The authors acknowledge many useful and enlightening discussions with S. G. Demos, C. W. Carr, and J. D. Bude. The authors thank G. Guss, D. Cross, R. Luthi, J. Vickers, J. Pryor, and W. Hollingsworth for assistance with experiments. This work was performed under the auspices of the U.S. Department of Energy by Lawrence Livermore National Laboratory under contract DE-AC52-07NA27344.

References

[1] Wong J, Ferriera JL, Lindsey EF, Haupt DL, Hutcheon ID, Kinney JH. Journal of Non-Crystalline Solids 2006;352:255.
[2] Carr CW, Cross DA, Norton MA, Negres RA. Opt Express 2011;19:A859.
[3] Negres RA, Liao ZM, Abdulla GM, Cross DA, Norton MA, Carr CW. Appl Opt 2011;50:D12.
[4] Suratwala TI, Miller PE, Bude JD, Steele WA, Shen N, Monticelli MV, Feit MD, Laurence TA, Norton MA, Carr CW, Wong LL. Journal of the American Ceramic Society 2011;94:416.
[5] Temple PA, Lowdermilk WH, Milam D. Applied Optics 1982;21:3249.
[6] Brusasco RM, Penetrante BM, Butler JA, Hrubesh LW. Proc SPIE 2002;4679:40.
[7] Nowak KM, Baker HJ, Hall DR. Appl Opt 2006;45:162.

[8] Skuja L. Journal of Non-Crystalline Solids 1998;239:16.
[9] Mullins WW. Journal of Applied Physics 1959;30:77.
[10] Genin FY, Salleo A, Pistor TV, Chase LL. J Opt Soc Am A 2001;18:2607.
[11] Li L, Xiang X, Zu X, Jiang X, Yuan X, Zheng W. Optik - International Journal for Light and Electron Optics 2011;122:1423.
[12] Bloembergen N. Applied Optics 1973;12:661.
[13] Carr CW, Radousky HB, Rubenchik AM, Feit MD, Demos SG. Physical Review Letters 2004;92:087401.
[14] Hirao K, Tomozawa M. J Am Ceram Soc 1987;70:43.
[15] Raman RN, Matthews MJ, Adams JJ, Demos SG. Optics Express 2010;18:9.
[16] Kucheyev SO, Demos SG. Appl Phys Lett 2003;82:3230.
[17] Vaccaro L, Cannas M, Radzig V, Boscaino R. Physical Review B 2008;78:075421.
[18] Feit MD, Rubenchik AM. Proceedings of SPIE 2003;4932:91.
[19] Wei C, He H, Deng Z, Shao J, Fan Z. Optical Engineering 2005;44:044202.
[20] Laurent Gallais PC, Jean-Luc Rullier. Optics Express 2009;17:23488.
[21] Raman RN, Negres RA, Demos SG. Optical Engineering 2011;50:013602.
[22] Yang ST, Matthews MJ, Elhadj S, Draggoo VG, Bisson SE. Journal of Applied Physics 2009;106:1031061.
[23] Rozenbaum O, Meneses DD, Auger Y, Chermanne S, Echegut P. Review of Scientific Instruments 1999;70:4020.
[24] Vignes RM, Soules TF, Stolken JS, Settgast RR, Elhadj S, Matthews MJ, Mauro J. Journal of the American Ceramic Society 2013;96:137.
[25] Laurence TA, Bude JD, Shen N, Feldman T, Miller PE, Steele WA, Suratwala T. Appl Phys Lett 2009;94:151114.
[26] Laurence TA, Bude JD, Shen N. MRS Proceedings 2011;1365.
[27] Nostrand MC, Weiland TL, Luthi RL, Vickers JL, Sell WD, Stanley JA, Honig J, Auerbach J, Hackel RP, Wegner PJ. Proc SPIE-Int Soc Opt Eng 2003;5273:325.
[28] Milam D, Lowdermilk WH, Rainer F, Swain JE, Carniglia CK, Hart TT. Appl Opt 1982;21:3689.
[29] Mann G, Vogel J, Zoheidi M, Eberstein M, Kruger J. Appl Surf Sci 2009;255:5519.
[30] Kirk CT. Physical Review B 1988;38:1255.
[31] Matthews MJ, Carr CW, Bechtel HA, Raman RN. Applied Physics Letters 2011;99:151109.
[32] Salleo A, Taylor ST, Martin MC, Panero WR, Jeanloz R, Sands T, Genin FY. Nature Materials 2003;2:796.
[33] Corning. HPFS(R) Fused Silica Standard Grade. 2003.
[34] Carr CW, Bude JD, DeMange P. Physical Review B 2010;82.
[35] Miller PE, Bude JD, Suratwala TI, Shen N, Laurence TA, Steele WA, Menapace J, Feit MD, Wong LL. Optics Letters 2010;35:2702.
[36] Ng A, Celliers P, Parfeniuk D. Phys Rev Lett 1987;58:214.
[37] Carr CW, Bude JD, Shen N, Demange P. Proceedings of the SPIE 2010;7842.
[38] DeMange P, Negres RA, Raman RN, Colvin JD, Demos SG. Physical Review B 2011;84.
[39] Demos SG, Negres RA, Raman RN, Rubenchik AM, Feit MD. Laser Photonics Rev 2013;7:444.
[40] Inglis CE. Transactions of the Institute of Naval Architecture 1913;55:219.
[41] Griffith AA. Phil Trans Roy Soc 1920;221A:163.
[42] Doremus RH. Journal of Applied Physics 1976;47:1833.
[43] Rountree CL, Kalia RK, Lidorikis E, Nakano A, Van Brutzel L, Vashishta P. Annual Review of Materials Research 2002;32:377.
[44] Matthews MJ, Stolken JS, Vignes RM, Norton MA, Yang S, Cooke JD, Guss GM, Adams JJ. Proceedings of the SPIE - The International Society for Optical Engineering 2009;7504.

[45] Shen N, Matthews MJ, Fair JE, Britten JA, Nguyen HT, Cooke D, Elhadj S, Yang ST. Appl Surf Sci 2010;256:4031.
[46] Lange FF, Gupta TK. Journal of the American Ceramic Society 1970;53:54.
[47] Gupta TK. Crack healing in Al_2O_3, MgO, and related materials. In: Kingery WD, editor. Advances in Ceramics. American Ceramic Society, 1984. p.750.
[48] Wang L, Ellison AJG, Ast DG. Journal of Applied Physics 2007;101:023530.
[49] Parikh NM. Journal of the American Ceramic Society 1958;41:18.
[50] Although this crack angle is somewhat arbitrary, the results derived from Eq (6) for angles in the range 40-44.9^o were essentially the same in terms of the position of the knee in strength vs δ.
[51] Hrma P, Han WT, Cooper AR. Journal of Non-Crystalline Solids 1988;102:88.
[52] Dahmani F, Burns SJ, Lambropoulos JC, Papernov S, Schmid AW. Optics Letters 1999;24:516.
[53] Dahmani F, Lambropoulos JC, Schmid AW, Papernov S, Burns SJ. Journal of Materials Research 1999;14:597.
[54] Scherer GW. Relaxation in Glass and Composites: Krieger, 1992.
[55] Brower KL, Myers SM. Applied Physics Letters 1990;57:162.
[56] Cartier E, Stathis JH, Buchanan DA. Applied Physics Letters 1993;63:1510.
[57] Collins CJ, Sampath AV, Garrett GA, Sarney WL, Shen H, Wraback M, Nikiforov AY, Cargill GS, Dierolf V. Applied Physics Letters 2005;86:031916.

FIGURES AND CAPTIONS

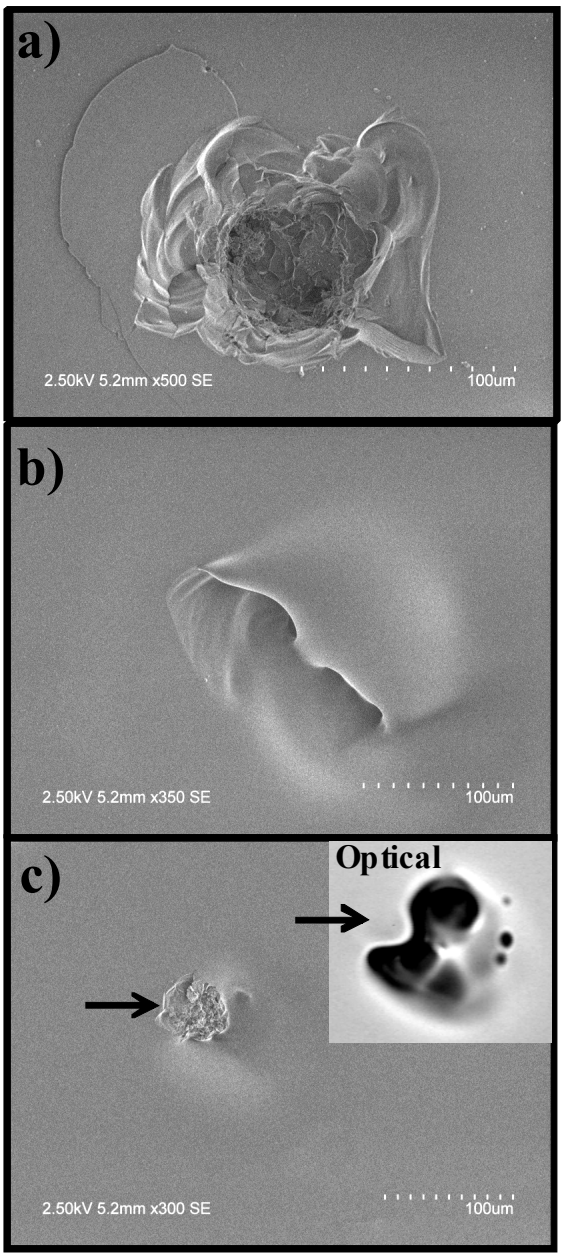

Figure 1. SEM images of 3 typical damage sites at various stages of annealing at three distinct annealing regimes: (a) a site after several damage growth exposures with no thermal treatment, (b) a site treated at 2250 K for 30 s, and c) another site treated at 1750 K for 100 s and then tested for damage threshold at 7.0 J/cm^2. Inset shows optical micrograph of site prior to damage test. Arrows indicate region where damage re-initiated and are co-registered.

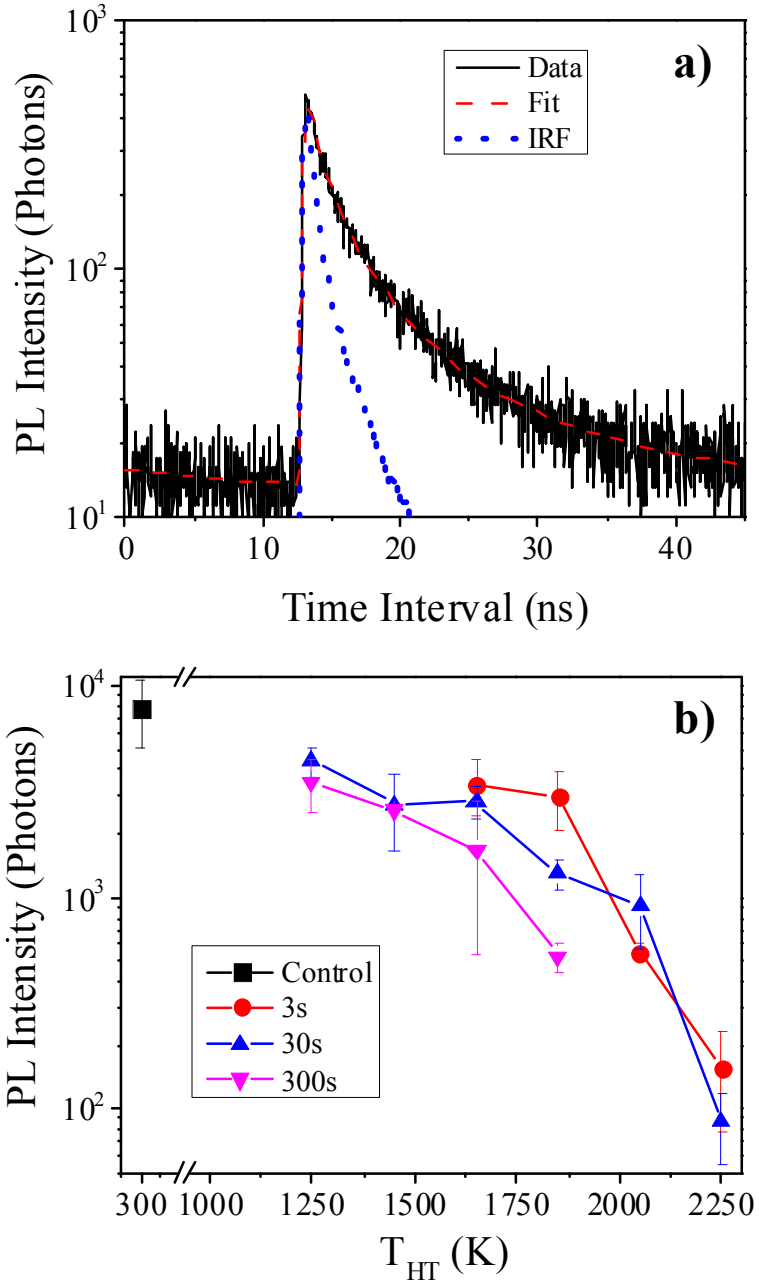

Figure 2. (a) Example of stretched-exponential fit to lifetime histogram of untreated site. (b) Total long-pass PL intensity under pulsed 405 nm excitation, excluding constant component from fits. Results from damage sites are shown over a range of CO_2 laser treatment temperatures for given exposure time.

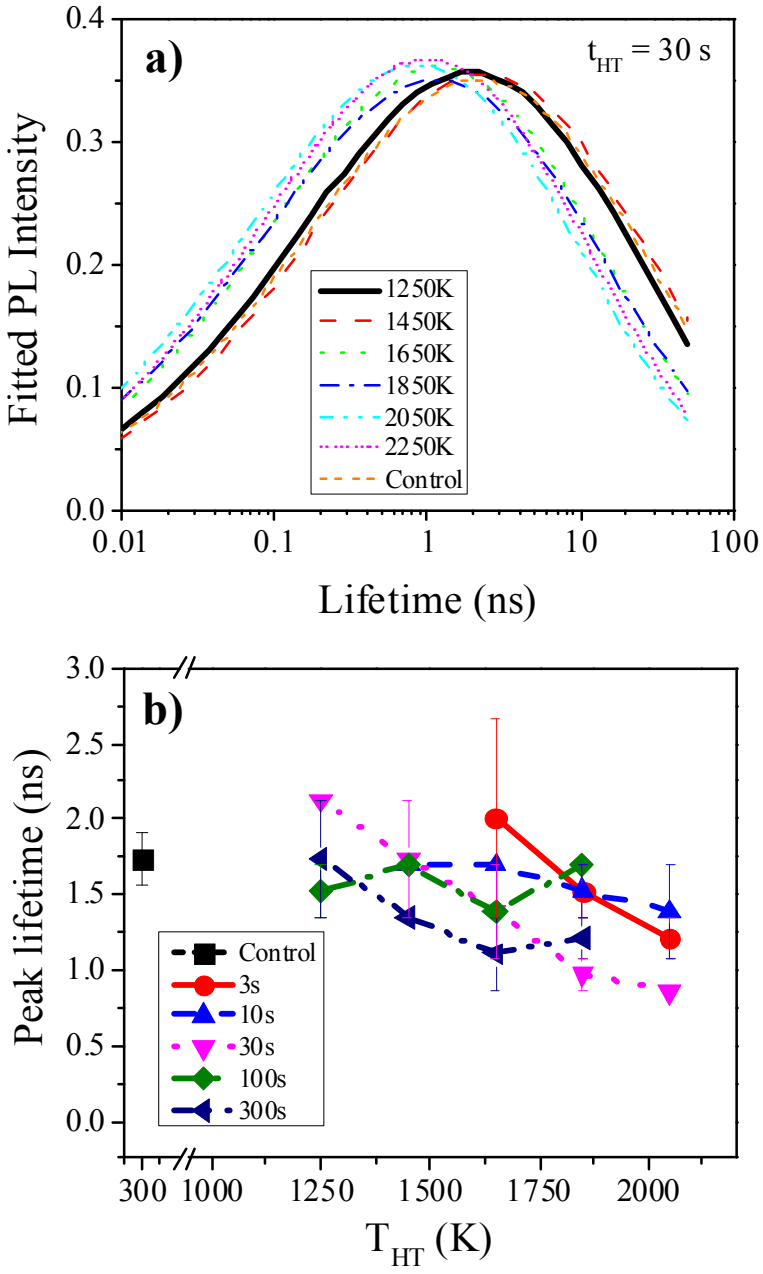

Figure 3. (a) Lifetime distributions derived using best-fit parameters obtained from sites treated at various temperatures for an exposure time of 30 s. (b) Value of lifetime at peak of distribution is shown for all treatment conditions.

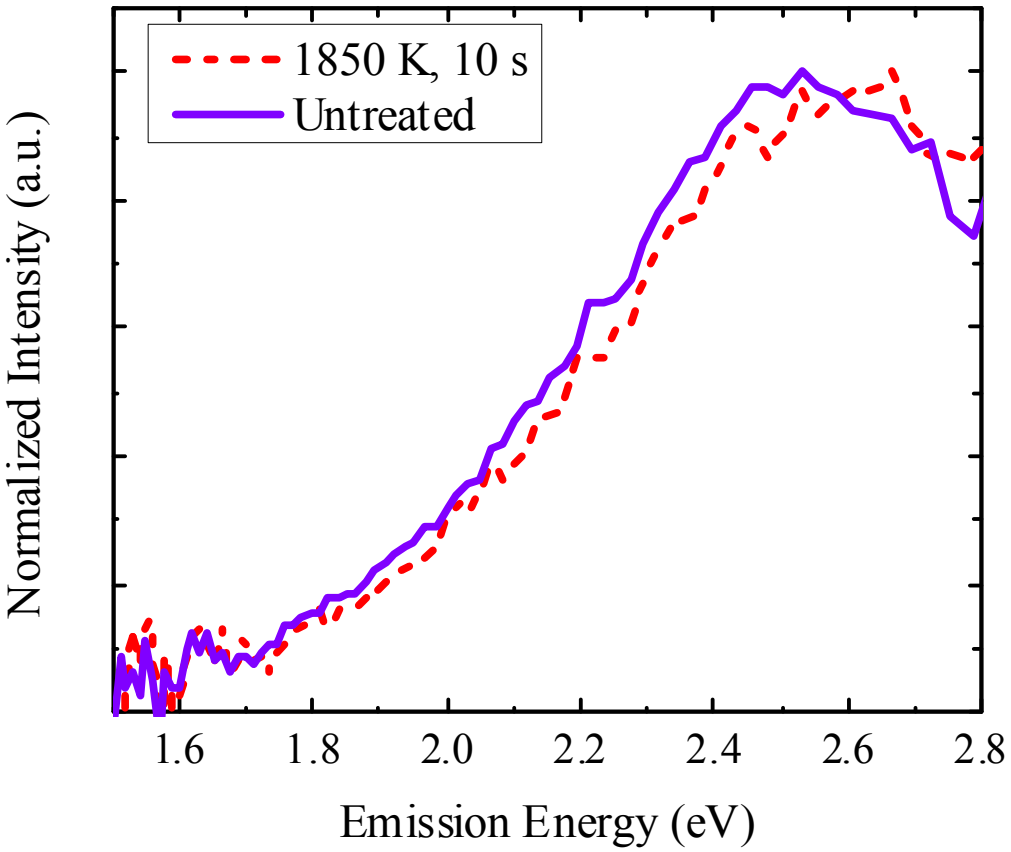

Figure 4: PL spectra under cw 405 nm excitation of an untreated vs. a treated damage site.

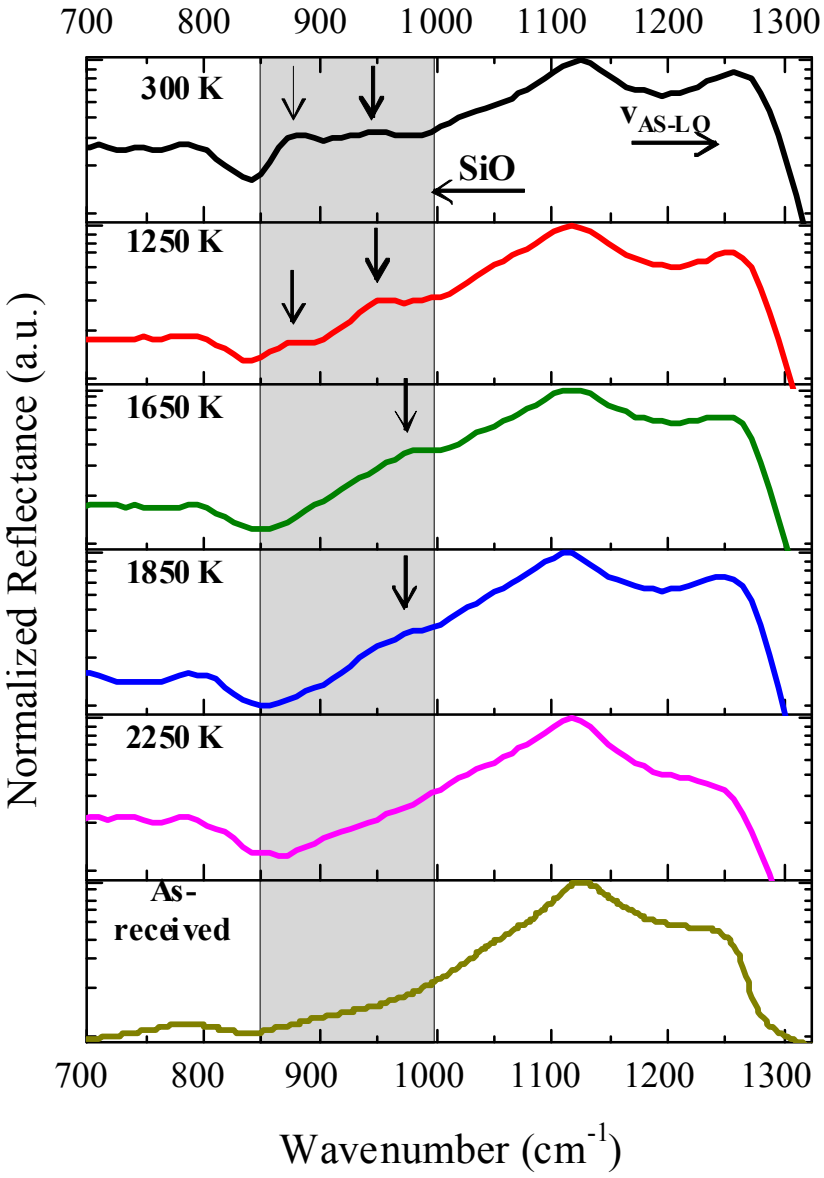

Figure 5: FTIR microreflectance spectra (semi-log scale) from core region of damage sites for different T_{HT} at t_{HT} = 30 s. Two modes associated with non-bridging oxygen are indicated with arrows in the SiO band. Shaded portion of spectrum corresponds to non-bridging oxygen modes. The dotted line indicates the position of ν_{AS-LO}, the asymmetric stretch longitudinal optic mode in silica.

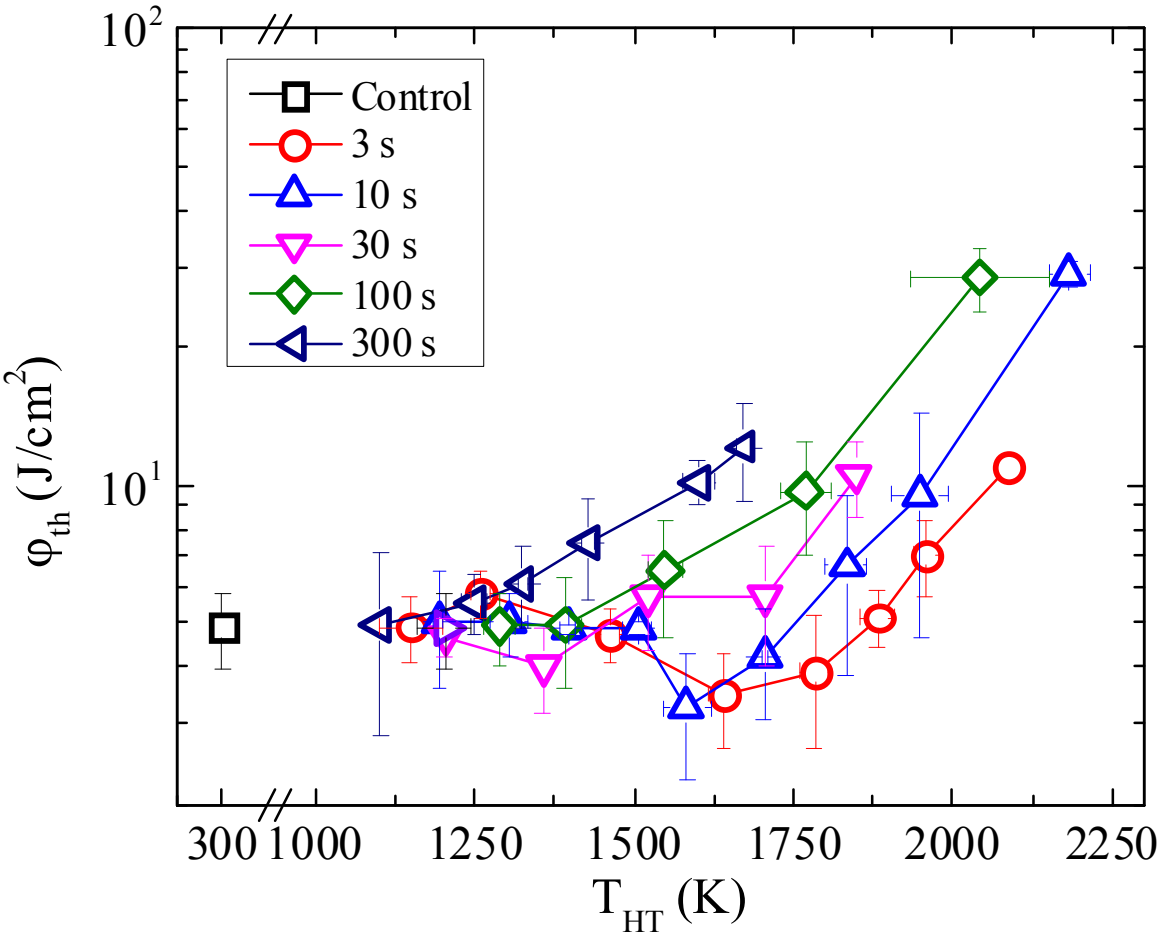

Figure 6: Damage threshold fluence of CO_2 laser-heated damage sites for the indicated treatment exposure times. Error bars represent ±1 standard deviation (n=8 for each data point).

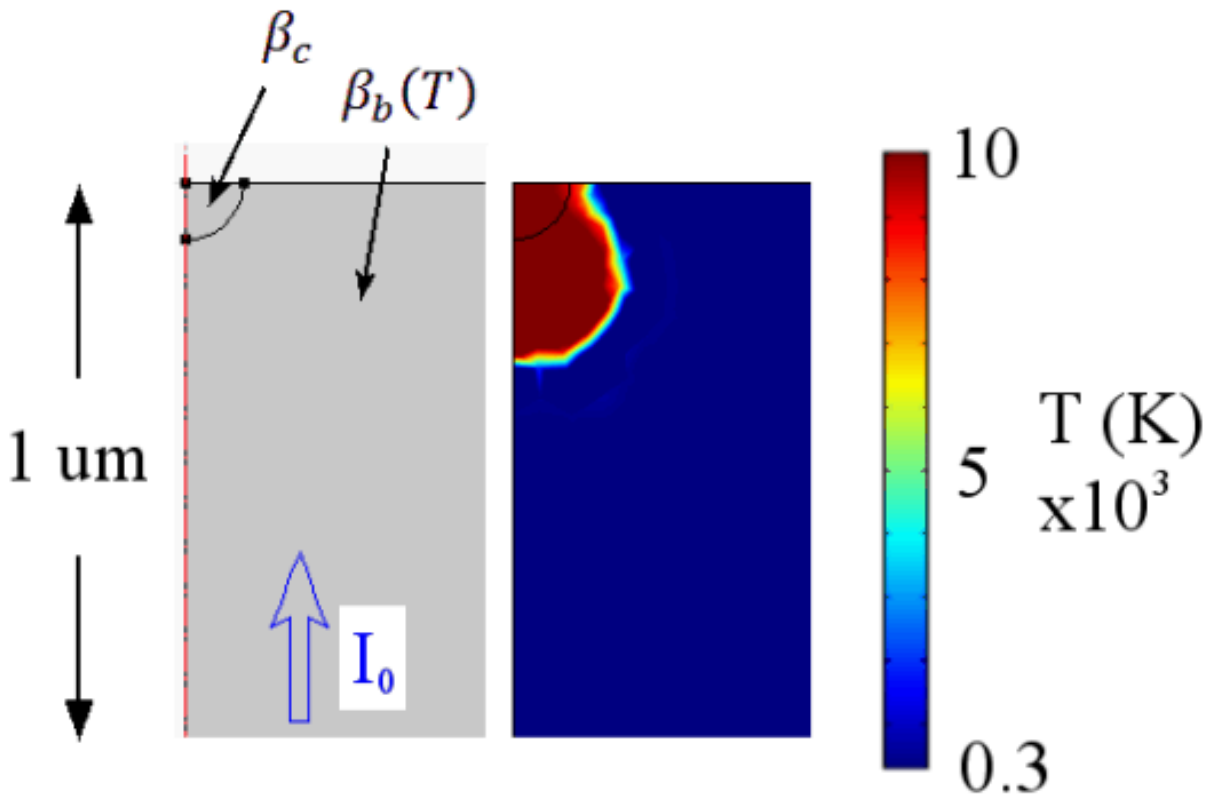

Figure 7: Simulation geometry near region of UV absorbing precursors at the exit surface indicated by an absorption coefficient . The calculated temperature map corresponds to t=2.5 ns after laser irradiation and for =1.5x10^3 cm^{-1} and I_0=20 J/cm^2.

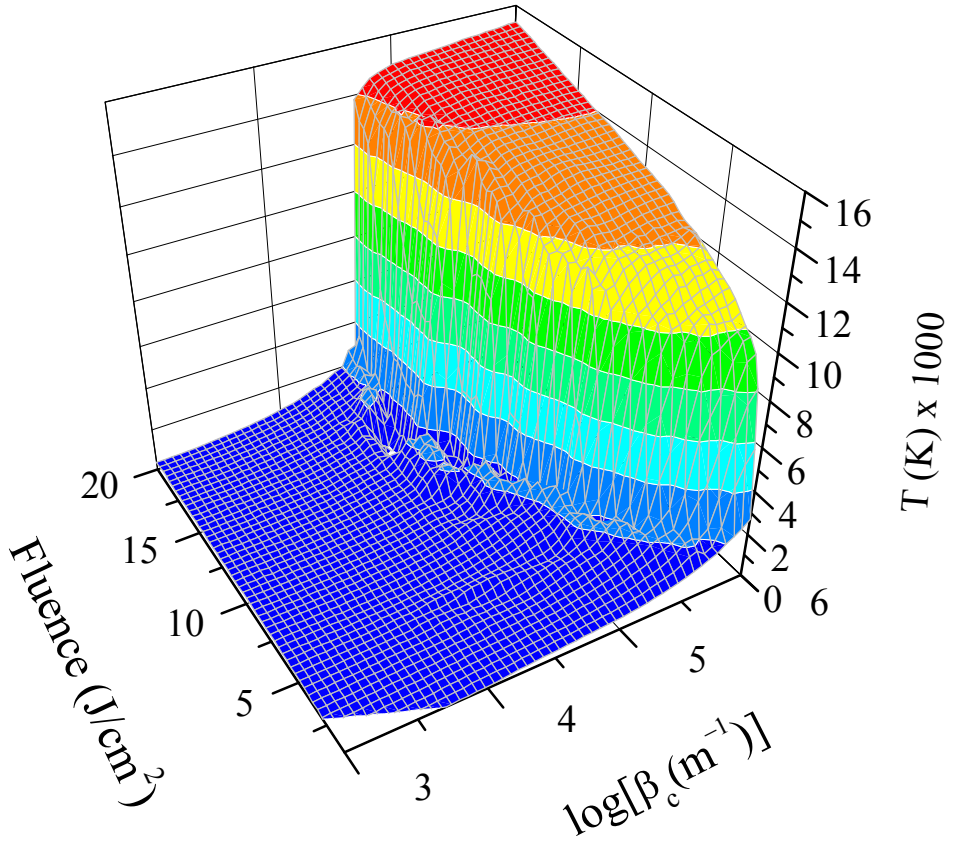

Figure 8: Calculated maximum axial temperature generated by a 5 ns pulse incident on a 100 nm absorbing hemisphere as a function of log(β_c) and laser fluence.

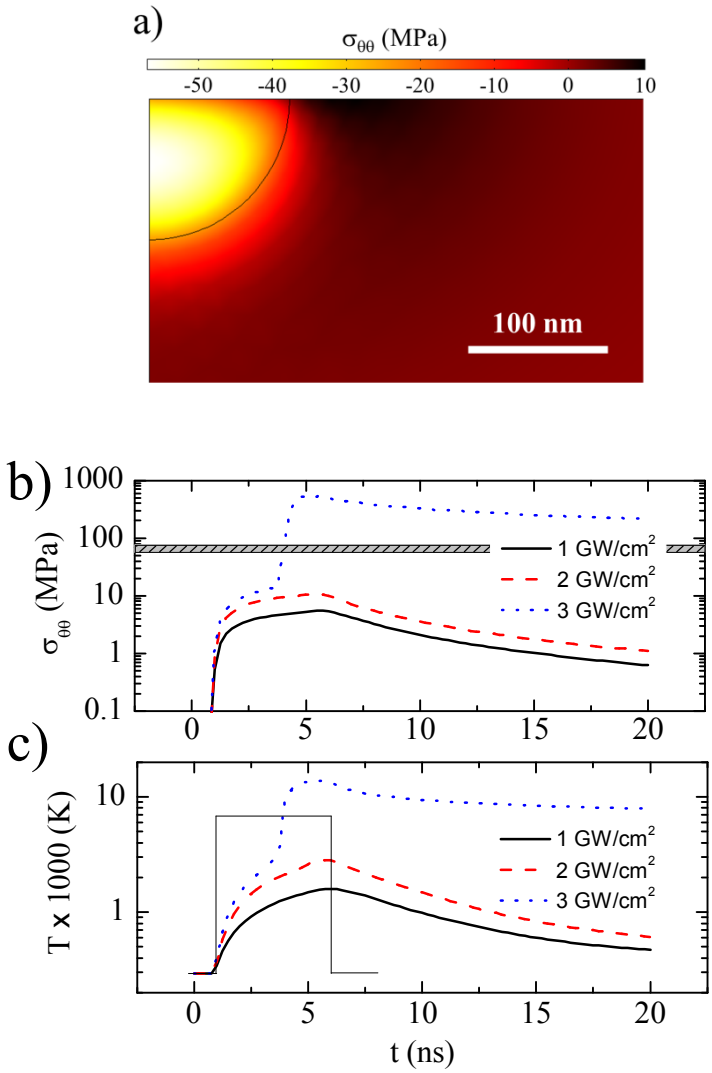

Figure 9: a) Principal hoop stress $\sigma_{\theta\theta}$ profile at the end of a 5 ns, 2 GW/cm^2 laser pulse incident on a $\beta_c=10^3$ cm^{-1} nano-absorber. Maximum (tensile) hoop stress $\sigma_{\theta\theta}$ (b) and temperature (c) over a 2x2 μm domain as a function of time and laser intensity for a 5 ns pulse incident on a 100 nm absorbing hemisphere. The horizontal band in b) denotes the expected range of critical stress for the damage sites studied here. The square trace in c) indicates the temporal position of the laser pulse.

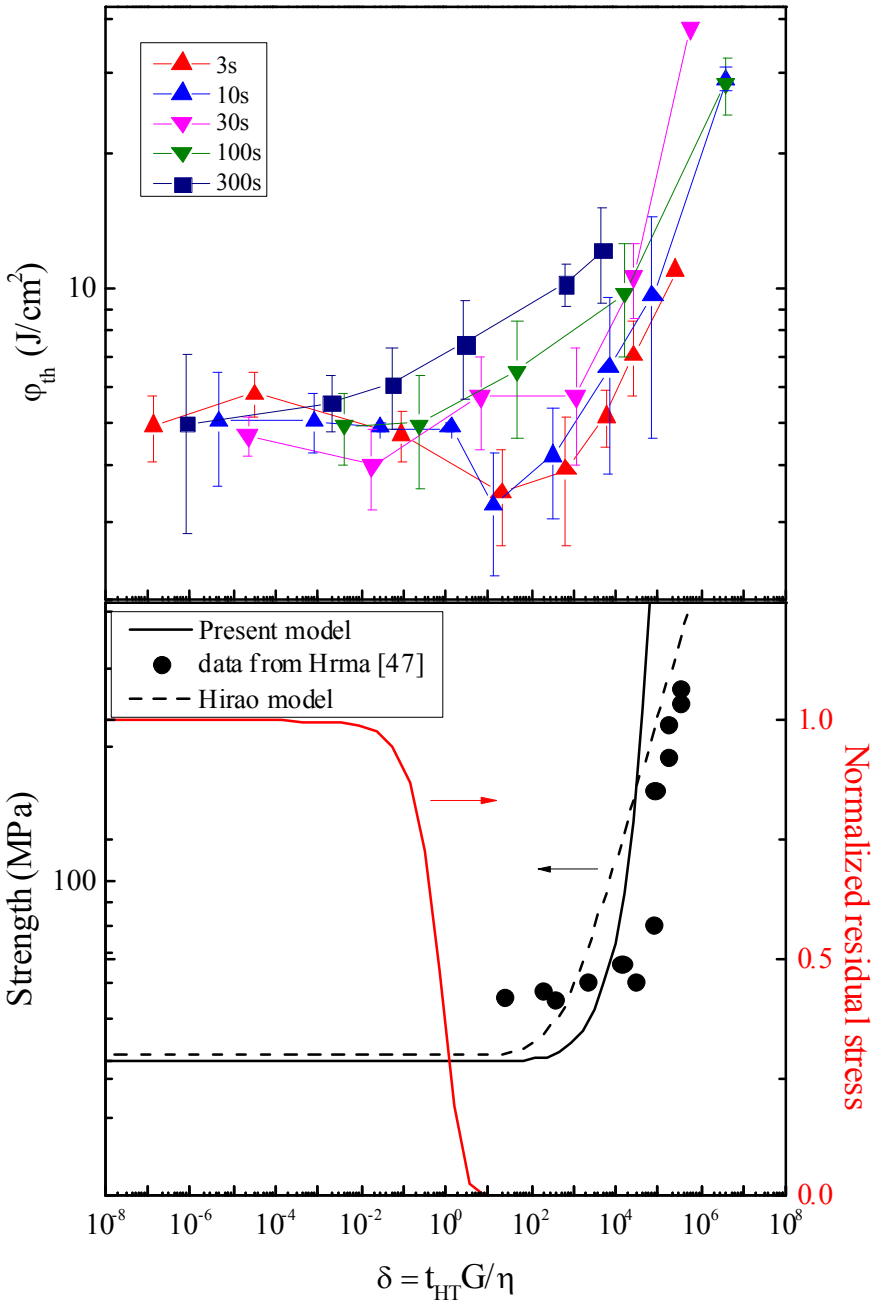

Figure 10: Threshold fluence (top graph) and stress predictions (bottom graph) plotted against normalized by CO_2 laser treatment time. The failure strength (stress) predicted by Hirao et al. (dashed line) is compared with our crack healing model (solid). Also shown in the bottom graph (right axis) is the predicted stress relaxation behavior for a rheologically simple glass.

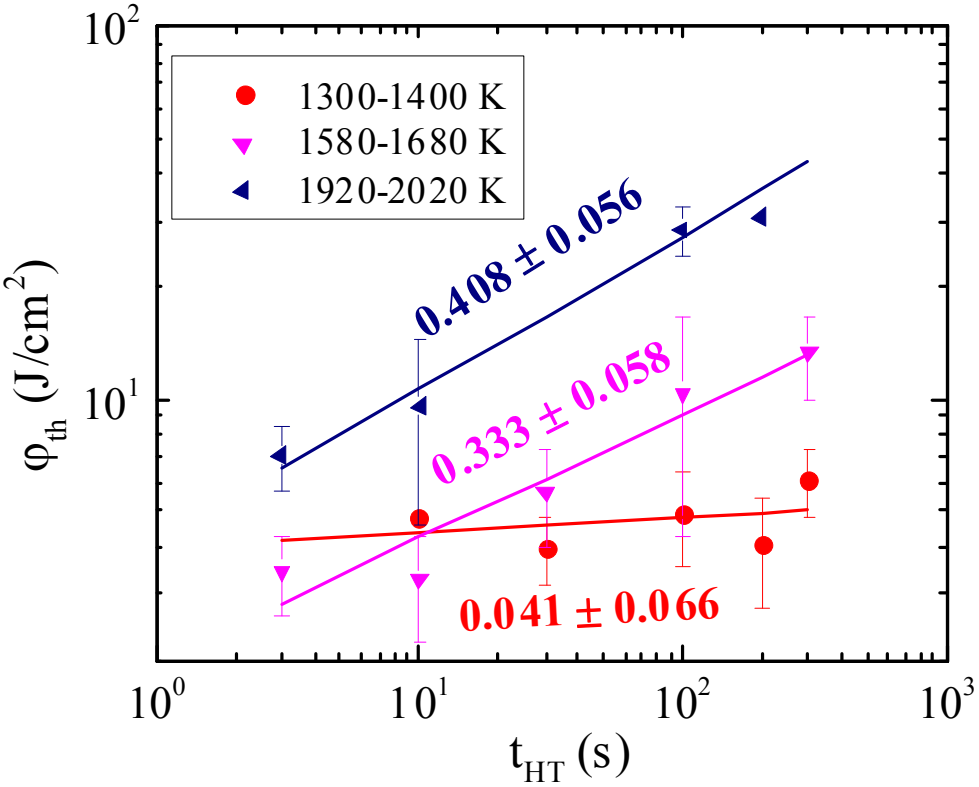

Figure 11: t_{HT}-dependence of φ_{th} (log-log scale) shown with results of corresponding linear regression for indicated ranges of T_{HT}.

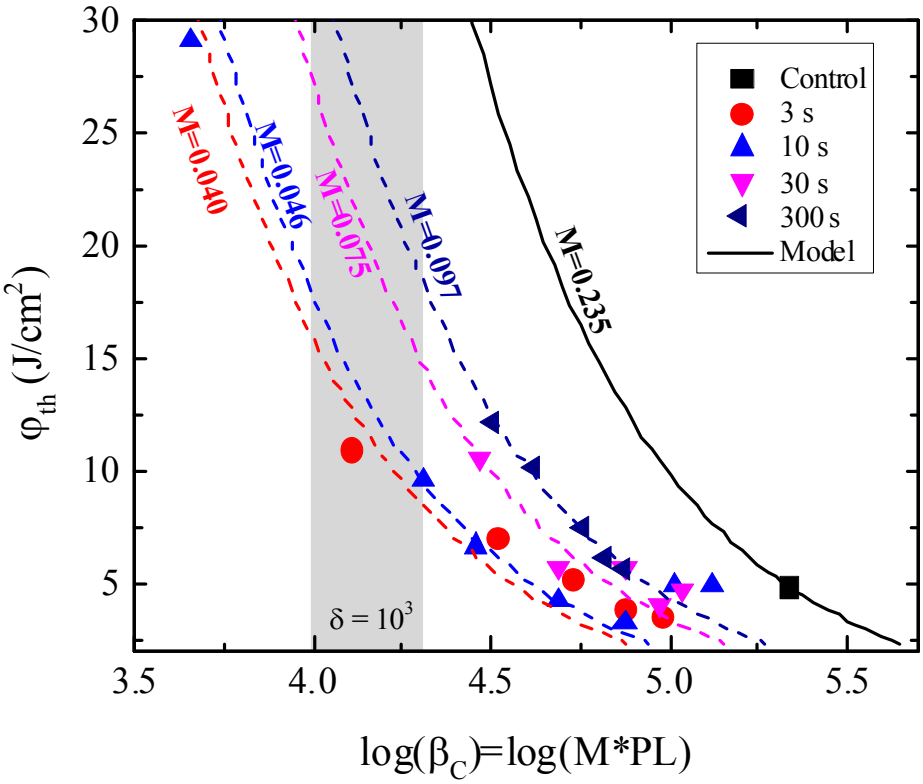

Figure 12: Comparison of the predicted T=3000 K isotherm (lines) to experimentally observed β_c-dependent enhancement in φ_{th}. Dotted lines represent fits to data for given best-fit parameter *M*. Shaded region indicates range of log(β_c) corresponding to $\delta = 10^3$ representing the demarcation between stress/defect relaxation regime and crack tip blunting regime of Fig. 10.